Materials Advances

ROYAL SOCIETY OF CHEMISTRY

PAPER

View Article Online
View Journal

Cite this: DOI: 10.1039/d6ma00196c

Porous $NiCo_2O_4$ nanorods as efficient catalysts for UV-assisted reduction of *p*-nitrophenol

Nanditha T K,[a] Mahi Varza Nataraajan,[a] Shreepooja Bhat,[a] Arun Kumar Thilipan,[b] Madhusudhan Alle,[c] Raghavendra K. G.[a] and Gurumurthy S. C. *[a]

Received 11th February 2026,
Accepted 2nd June 2026

DOI: 10.1039/d6ma00196c

rsc.li/materials-advances

The catalytic reduction of nitroaromatic pollutants using transition metal oxides has attracted increasing attention as an alternative to noble-metal-based catalysts. Among these materials, spinel $NiCo_2O_4$ has emerged as a promising catalyst owing to its mixed-valence redox chemistry, good electrical conductivity, and low cost. However, the relationship between its morphological characteristics and catalytic performance remains insufficiently understood. In this work, $NiCo_2O_4$ nanostructures were synthesized through a polyvinylpyrrolidone (PVP)-assisted hydrothermal method followed by thermal annealing at different temperatures to investigate the influence of morphology on *p*-nitrophenol (PNP) reduction. The optimised sample exhibited an optical bandgap of approximately 2.9 eV and achieved 99.5% conversion of PNP under UV irradiation. The enhanced catalytic performance is attributed to the nanorod morphology, improved active surface area, and efficient interfacial electron transfer. The catalyst retained more than 97% of its activity after five catalytic cycles, demonstrating good stability. These results demonstrate the potential of morphology-engineered $NiCo_2O_4$ nanorods for catalytic reduction of nitroaromatic pollutants.

1. Introduction

The persistent discharge of synthetic and organic pollutants into aquatic systems by textile, leather, paper and medical industries poses serious ecological and health hazards. These pollutants, particularly nitroaromatic compounds such as *p*-nitrophenol (PNP), are among the most hazardous, and are listed as priority pollutants by the US Environmental Protection Agency due to their toxicity, carcinogenicity, and resistance to natural degradation. Alongside these, azo dyes and other nitro-aromatic compounds are chemically stable, non-biodegradable, and often toxic or carcinogenic. Conventional wastewater treatment methods like coagulation, flocculation, or biological degradation often fall short in addressing such pollutants due to incomplete breakdown, high operational costs, or secondary waste generation.[1,2]

To address these limitations, several advanced treatment approaches like photocatalysis have been investigated. Zinc oxide nanoparticles have been reported to degrade methylene blue with over 90% efficiency under visible light within 1–2 hours.[3] Hydrothermally synthesized Titanium dioxide nanomaterials have demonstrated complete degradation of dyes under ambient sunlight conditions in under 40 minutes,[4] while enzyme-based membrane reactors have achieved up to 100% removal of azo dyes under mild operating conditions.[5] Microalgae-based biosorption and polysaccharide hydrogel composites have also emerged as promising alternatives, offering high adsorption capacities and excellent reusability.[6,7] Recent studies have also explored diverse remediation strategies, including organic dye degradation using 6,13-pentacenequinone/zinc oxide nanocomposites,[8] removal of lead and copper using Bael fruit shell adsorbents,[9,10] and pollutant removal using Fe-doped hydroxyapatite encapsulated with alginate.[11] Such studies highlight the need for efficient, low-cost, and reusable materials for wastewater treatment.[12–18] However, most of these systems target dye molecules under oxidative or adsorptive mechanisms and are not directly applicable to the selective chemical transformation of nitroaromatic compounds such as PNP. For PNP specifically, catalytic reduction to *p*-aminophenol (PAP) using $NaBH_4$ as a reductant offers a more targeted route, converting a toxic nitroaromatic into a useful chemical intermediate with well-defined reaction kinetics.[19,20]

Nanostructured transition metal oxides have attracted growing attention as cost-effective alternatives to noble metal catalysts such as Au, Ag, and Pd.[21–23] Their redox-active metal centers facilitate electron transfer between the reductant and the substrate, which is the rate-determining step in $NaBH_4$-assisted PNP reduction. In this context, bimetallic oxides offer an advantage over single-metal oxides because the presence of two redox-active metal centers creates a synergistic electronic environment that improves electron transfer efficiency. Nickel cobaltite ($NiCo_2O_4$) is one such earth-abundant bimetallic oxide, where the coexistence of Ni^{2+}/Ni^{3+} and Co^{2+}/Co^{3+} redox

[a] Manipal Institute of Technology, Manipal Academy of Higher Education, Manipal, India. E-mail: gurumurthy.sc@manipal.edu
[b] Dr. Bansi Dhar Institute, Gurugram-122015, India
[c] Department of Chemistry, The University of Memphis, Memphis, TN 38152, USA

pairs provides enhanced charge transport and structural stability, and has been shown to be active for PNP reduction.[6,24]

However, the catalytic performance of $NiCo_2O_4$ is strongly dependent on its morphology. One-dimensional (1D) nanostructures such as nanorods expose a higher density of reactive crystal facets, provide lower diffusion resistance for reactants, and support more efficient electron transport along the rod axis than aggregated particles or nanoflakes. These structural advantages directly translate to higher reaction rates in $NaBH_4$-assisted reduction.[25,26]

However, prior studies have tested single catalyst morphology under dark conditions only, and a systematic comparison of morphology-dependent catalytic activity combined with UV-assisted reduction has not been reported for this material. In this work, $NiCo_2O_4$ nanorods are synthesized *via* a PVP-directed hydrothermal method followed by thermal annealing. The catalytic activity of the resulting nanorods is evaluated using the model reduction of PNP in the presence of sodium borohydride ($NaBH_4$). The influence of annealing temperature on crystallinity, morphology, and catalytic efficiency is systematically examined to establish a clear structure–function relationship. Additionally, the contribution of 254 nm UV irradiation to the $NaBH_4$-assisted reduction pathway is quantified.

2. Experimental

2.1. Chemicals used

p-Nitrophenol ($C_6H_5NO_3$), sodium borohydride ($NaBH_4$, 97%, extra pure), and nickel nitrate hexahydrate ($Ni(NO_3)_2{\cdot}6H_2O$, 99% AR) were sourced from Loba Chemie Pvt. Ltd and cobalt nitrate hexahydrate ($Co(NO_3)_2{\cdot}6H_2O$, 98%) was procured from Merck Life Science Pvt. Ltd. Polyvinylpyrrolidone (PVP) was purchased from Sigma Aldrich. Milli-Q water was used to prepare all chemicals. No additional purification was performed on the chemicals used.

2.2. Synthesis of NiCo-LDH

NiCo bimetallic layered double hydroxide (NiCo-LDH) was synthesized *via* a simple hydrothermal method using nitrate precursors. In a typical synthesis, nickel nitrate hexahydrate ($Ni(NO_3)_2{\cdot}6H_2O$, 87.27 mg) and cobalt nitrate hexahydrate ($Co(NO_3)_2{\cdot}6H_2O$, 145.88 mg) were dissolved in 30.0 mL of deionized water to form Solution A. In parallel, polyvinylpyrrolidone (PVP) (1 g) was dissolved in 30.0 mL of deionized water to prepare Solution B. Solution A was slowly added to Solution B under continuous stirring, and the resulting mixture was stirred for an additional 15 minutes to ensure uniform mixing.

The homogeneous mixture was transferred into a 100 mL Teflon-lined stainless-steel autoclave and heated at 150 °C for 12 hours in a hydrothermal reactor. After natural cooling to room temperature, the resulting precipitate was collected by centrifugation at 8000 rpm, washed thoroughly with deionized water and ethanol to remove unreacted species and excess PVP, and then dried in a hot air oven at 60 °C for 12 hours. The as-synthesized material exhibited a rod-like morphology and corresponded to a layered Ni–Co hydroxide phase (LDH), which served as the precursor for $NiCo_2O_4$ nanorods (Scheme 1).

2.3. Synthesis of $NiCo_2O_4$ nanostructures

The as-prepared NiCo-LDH powder was thermally treated to obtain spinel $NiCo_2O_4$ nanorods. The dried LDH sample was placed in a ceramic crucible and annealed in a muffle furnace at three different temperatures: 300 °C (NCO-3), 400 °C (NCO-4), and 500 °C (NCO-5) for 3 hours each (Scheme 1). Additionally, a bare $NiCo_2O_4$ sample (NCO-B) was prepared under identical conditions but without using PVP as a structure-directing agent. Thermal decomposition of the LDH phase during annealing led to the removal of interlayer water, hydroxyl groups, and nitrate ions, thereby promoting the formation of the crystalline spinel $NiCo_2O_4$ structure. The synthesized samples, their annealing conditions, and the corresponding dominant morphologies are summarized in Table 1.

2.4. Catalytic activity

The catalytic activity of the synthesized catalyst was evaluated through the reduction of PNP using $NaBH_4$ as the reducing agent. In a typical experiment, 50 μL of 0.005 M PNP solution was added to 2.5 mL of distilled water in a quartz cuvette. Subsequently, 100 μL of catalyst dispersion (prepared by dispersing 50 mg of catalyst in 20 mL distilled water) was introduced, followed by the addition of 80 μL of freshly prepared 0.5 M $NaBH_4$ solution to initiate the reaction. The reaction progress was monitored in real time using UV-visible spectroscopy by recording the decrease in the characteristic absorption peak of PNP at regular time intervals.

For UV-assisted catalytic experiments, the reaction mixture was irradiated using a 254 nm UV lamp (8 W, Philips) placed

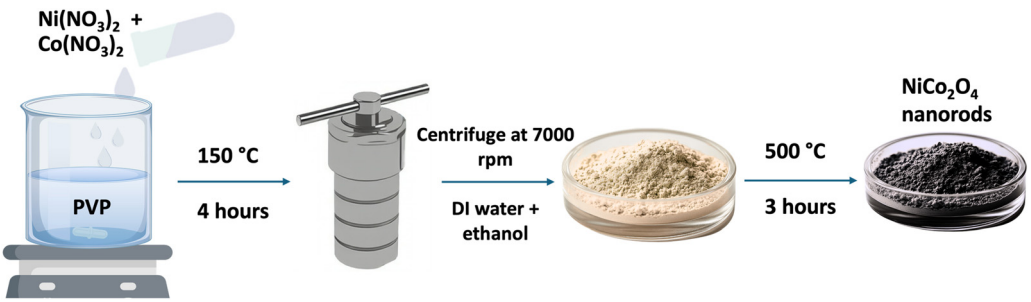

Scheme 1 Synthesis of $NiCo_2O_4$ nanorods (NCO-5).

Table 1 Summary of sample designations, synthesis conditions, and morphology

Sample	PVP	Annealing temperature (°C)	Dominant morphology
NCO-B	No	500	Aggregated particles
NCO-3	Yes	300	Urchin-like structures
NCO-4	Yes	400	Urchin-like structures
NCO-5	Yes	500	Nanorods (avg. diameter: 44 nm, avg. length: 220 nm)

inside a homemade UV irradiation chamber, with the distance between the lamp and the quartz cuvette maintained at approximately 6 cm. All experiments were performed under continuous stirring to ensure uniform dispersion of the dye solution during irradiation.

To further investigate the reaction kinetics, the experimental data were analysed using a pseudo-first-order kinetic model, as described by eqn (1) and (2):

$$\text{Reduction percentage} = \left(\frac{A_0 - A_t}{A_0}\right) \times 100 \quad (1)$$

$$\ln\left(\frac{A_t}{A_0}\right) = -kt \quad (2)$$

A_0 and A_t represent the initial absorbance and the absorbance at time t, respectively. The parameter k denotes the apparent first-order rate constant.

All catalytic experiments were performed independently in triplicate under identical experimental conditions, and the reported values represent the average of three measurements. Error bars in the corresponding plots represent the standard deviation of the measurements.

2.5. Characterization

Surface morphology was studied using Field Emission Scanning Electron Microscopy (FESEM), equipped with an EDAX detector from TESCAN and Bruker. Structural studies were carried out using X-ray diffraction (XRD; Rigaku ultima IV). Optical properties were measured using a SHIMADZU-1900i UV-visible spectrophotometer. XPS curve fitting was performed using KherveFitting software.[27] X-ray photoelectron spectroscopy (XPS) measurements were carried out using a Thermo Scientific K-Alpha system to analyze the surface chemical composition and oxidation states of the constituent elements. Photoluminescence (PL) studies were performed with a JASCO FP-8500 spectrofluorometer to investigate the recombination characteristics of photogenerated charge carriers. Electrochemical impedance spectroscopy (EIS) and Mott–Schottky analyses were performed using an OrigaFlex OGF + 01A electrochemical workstation employing a conventional three-electrode setup with Hg/HgO as the reference electrode. Brunauer–Emmett–Teller (BET) analysis of the samples was done using a MICTROTRAC-BELSORP MINI X.

3. Results and discussion

3.1. Morphological analyses

The morphological evolution of $NiCo_2O_4$ nanorods annealed at different temperatures was examined using FESEM, as depicted in Fig. 1. At 300 °C and 400 °C, the nanorods exhibited a radiating, urchin-like assembly. Upon annealing at 500 °C, the

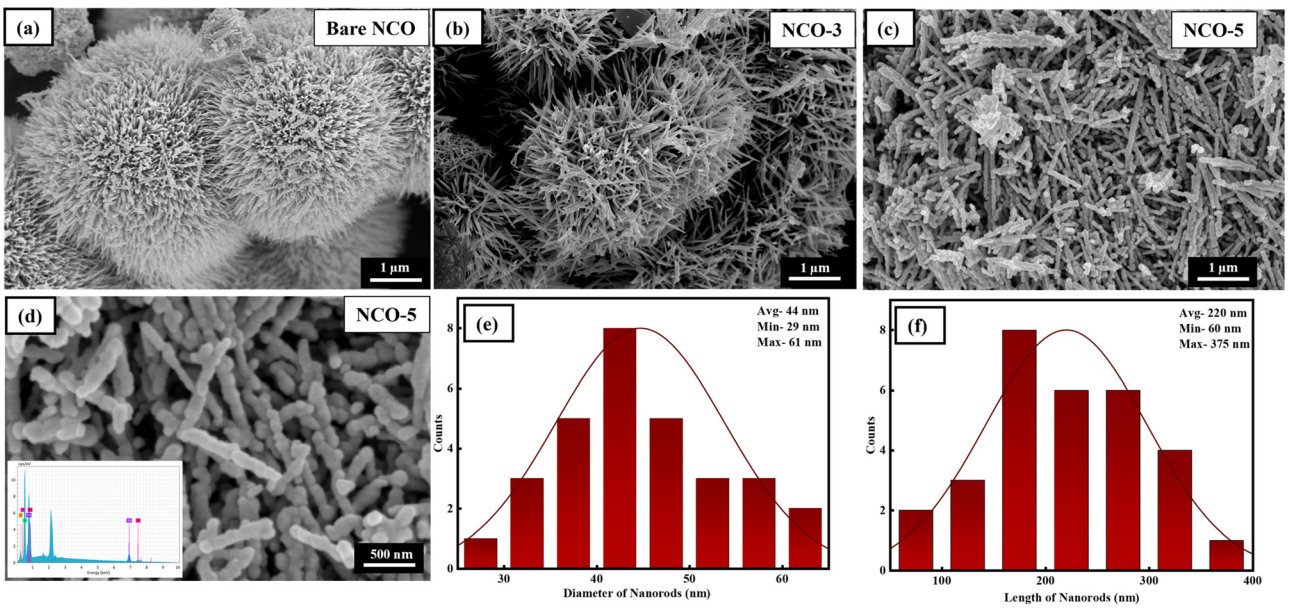

Fig. 1 FESEM images of (a) NCO-B, (b) NCO-3, and (c and d) NCO-5, revealing morphological evolution with annealing temperature (inset: EDS spectrum of NCO-5 showing elemental composition). (e and f) Nanorod size distribution histograms of NCO NRs.

morphology transformed significantly, with individual nanorods becoming more uniformly distributed, exhibiting improved aspect ratios and smoother surfaces. The average diameter of these rods was 44 nm. The rod length ranged from 60 nm to 375 nm, with an average of 220 nm.

The observed morphological evolution can be attributed to enhanced atomic diffusion and recrystallization at elevated annealing temperatures. At lower temperatures (300–400 °C), insufficient thermal energy leads to the formation of densely packed, radiating urchin-like assemblies. Increasing the annealing temperature to 500 °C promotes grain growth, reduces surface defects, and improves crystallinity, resulting in more distinct, uniformly distributed nanorods with smoother surfaces and higher aspect ratios. In addition, thermal decomposition of residual precursor species and hydroxides during annealing further contribute to the restructuring of the nanorod architecture. Similar annealing-induced morphological transformations have been reported in $NiCo_2O_4$ and other metal oxide nanostructures. These observations are consistent with earlier studies reporting similar nanorod morphologies and their thermal evolution.[28,29]

3.2. Structural analysis

The phase evolution and crystallinity of the synthesized $NiCo_2O_4$ nanorods annealed at 300 °C, 400 °C, and 500 °C were systematically investigated using XRD, as presented in Fig. 2 (b). The as-prepared NiCo-LDH precursor exhibited broad, low-intensity reflections characteristic of layered hydroxide structures with poor crystallinity.[30] Upon annealing at 300 °C (NCO-3), distinct reflections appeared at $2\theta = 30.76°$, 36.68°, 37.68°, 43.84°, 58.90°, and 63.98°, corresponding to the (220), (311), (222), (400), (511), and (440) planes of cubic spinel $NiCo_2O_4$ (JCPDS No. 20-0781), confirming phase formation.[28] Annealing at 400 °C (NCO-4) resulted in sharper peaks at $2\theta = 30.64°$, 36.74°, 38.08°, 44.42°, 59.14°, and 64.78°, indicating improved crystallinity and lattice development. At 500 °C (NCO-5), the XRD profile displayed highly resolved peaks at $2\theta = 18.86°$, 31.06°, 36.72°, 38.22°, 44.66°, 55.46°, 59.38°, and 64.94°, corresponding to the (111), (220), (311), (222), (400), (422), (511), and (440) planes, indicating the formation of a well-crystallized spinel $NiCo_2O_4$ phase. These results align with prior reports on thermal transformation and lattice ordering of $NiCo_2O_4$.[29,31] The systematic peak shift to higher angles with increasing annealing temperature reflects lattice contraction and internal strain relaxation, attributed to dehydroxylation and atomic rearrangement during phase transformation.

3.3. Optical analysis

The optical properties of the optimized $NiCo_2O_4$ nanorods (NCO-5) were investigated by ultraviolet visible absorption spectroscopy, and the resulting spectrum is shown in Fig. 2(a). The NCO-5 sample exhibits a broad, monotonically decreasing absorption profile extending from the ultraviolet into the visible region, with a pronounced absorption shoulder in the 250–350 nm range. This broad-band absorption is characteristic of spinel nickel cobaltite materials and arises from a combination

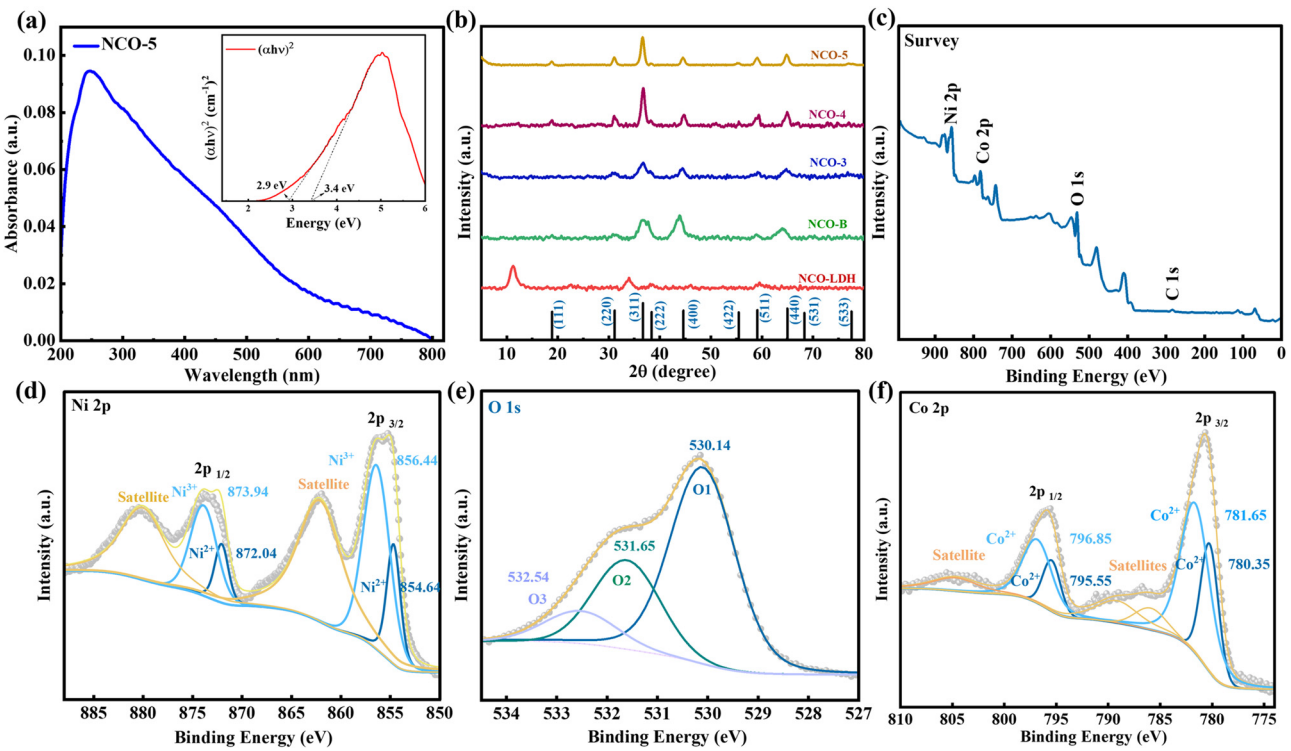

Fig. 2 (a) UV-vis absorption spectrum of NCO-5, with the inset showing the corresponding Tauc plot used for estimation of the optical bandgaps. (b) XRD patterns of NCO-LDH, NCO-B, NCO-3, NCO-4, and NCO-5 compared with standard cubic spinel $NiCo_2O_4$ (JCPDS No. 20-0781). (c) XPS survey spectrum of NCO-5. High-resolution XPS spectra of (d) Ni 2p, (e) O 1s, and (f) Co 2p for NCO-5.

of charge transfer transitions between oxygen 2p and metal 3d states and d–d transitions associated with nickel and cobalt cations in octahedral and tetrahedral sites, as reported in previous studies on $NiCo_2O_4$ nanostructures prepared *via* solution-based routes.[32] The strong absorption in the ultraviolet region indicates that NCO-5 can efficiently harvest high-energy photons from the 254 nm UV source (8 W, λ = 254 nm) used in the catalytic experiments, thereby providing a high density of photo-excited charge carriers that can participate in the reduction of PNP in the presence of $NaBH_4$.[33]

The inset of Fig. 2(a) presents the Tauc plot, where the quantity $(\alpha h\nu)^2$ is plotted as a function of photon energy. The Tauc formalism assumes a direct allowed electronic transition and is frequently applied to spinel metal oxides such as $NiCo_2O_4$ because their optical response is dominated by direct band-to-band transitions, as demonstrated in earlier reports on $NiCo_2O_4$ thin films and nanopowders.[34] In the present case, two linear regions can be resolved in the Tauc plot, and linear extrapolation of these regions to the energy axis yields two apparent optical transition energies of approximately 2.9 eV and 3.4 eV.[35]

The lower energy transition around 2.9 eV can be attributed to the fundamental bandgap associated with charge transfer between the oxygen 2p band and the hybridized nickel cobalt 3d conduction band, which is consistent with literature band-gap values for $NiCo_2O_4$ nanostructures typically reported in the range from 2.0 to 2.5 eV for bulk-like samples and up to about 3.0 eV for size-confined particles.[36] The slightly higher value of 2.9 eV observed for NCO-5 is consistent with nanosize effects from the nanorod morphology and the annealing temperature, as nanostructured $NiCo_2O_4$ commonly exhibits blue-shifted bandgaps relative to bulk values.[37]

The second transition at approximately 3.4 eV corresponds to higher energy charge transfer processes involving deeper-lying oxygen states and metal-centered orbitals. The presence of two distinct optical transitions is consistent with multiple bandgaps reported for $NiCo_2O_4$ nanostructures, such as 2.06/3.63 eV in core-ring nanoplatelets[37] and similar dual features in urchin-like microspheres.[38]

The strong absorption extending to 254 nm (4.88 eV photon energy) is particularly significant for this study, as the catalytic experiments employed a source emitting predominantly at 254 nm.[39] Since this photon energy exceeds both observed transitions (2.9 eV and 3.4 eV), each absorbed photon provides sufficient energy for band-to-band excitation and populates higher electronic states, enhancing the driving force for charge transfer in UV-assisted PNP reduction.[40]

3.4. XPS analyses

XPS analyses was carried out to investigate the surface chemical composition and oxidation states of NCO-5, and the corresponding spectra are shown in Fig. 2(c–f). The survey spectrum confirmed the presence of Ni, Co, and O, with no detectable impurity peaks.

The high-resolution Ni 2p spectrum was deconvoluted using Voigt fitting profiles after Shirley background subtraction. The fitted peaks centred at 854.66 and 872.06 eV correspond to Ni^{2+} $2p^{3/2}$ and Ni^{2+} $2p^{1/2}$, respectively, while the peaks located at 856.38 and 873.88 eV are assigned to Ni^{3+} species. Satellite peaks observed at 862.10 and 880.03 eV further confirm the mixed-valence nature of nickel in the spinel framework. The fitted Ni 2p peaks exhibited full width half maximum (FWHM) values in the range of 1.65–3.16 eV, whereas the satellite peaks showed broader FWHM values of approximately 5.2–5.3 eV.

The Co 2p spectrum also exhibited characteristic mixed-valence Co^{2+}/Co^{3+} features. The Co^{2+} peaks located at 780.35 eV (Co $2p^{3/2}$) and 795.46 eV (Co $2p^{1/2}$), together with the Co^{3+} peaks centred at 781.95 and 797.07 eV, confirm the coexistence of multiple cobalt oxidation states within the $NiCo_2O_4$ structure. In addition, shake-up satellite peaks observed at 787.11 and 804.63 eV further support the spinel nature of the material. The fitted Co 2p peaks exhibited FWHM values in the range of 2.08–2.60 eV, while the satellite peaks showed broader FWHM values of approximately 5.0–5.7 eV.

The O 1s spectrum was deconvoluted into three components centred at 530.10, 531.61, and 532.52 eV with FWHM values of 1.53, 1.56, and 1.69 eV, respectively. The peak at 530.10 eV corresponds to lattice oxygen associated with the $NiCo_2O_4$ framework, while the component at 531.61 eV is attributed to defect-related oxygen species. The higher binding energy peak at 532.52 eV is associated with surface-adsorbed oxygen-containing species and hydroxyl groups. The relative concentrations obtained from O 1s fitting were 62.3%, 26.8%, and 10.9%, respectively, indicating the predominance of lattice oxygen together with a noticeable contribution from surface defect-related oxygen species.

All spectra were fitted using constrained spin–orbit splitting and area ratios for the corresponding doublets. The satisfactory fitting quality and quantitative deconvolution support the successful formation of mixed-valence spinel $NiCo_2O_4$ nanorods.

In spinel $NiCo_2O_4$, the Ni 2p and Co 2p binding energies are primarily governed by the intrinsic mixed-valence states of Ni and Co within the spinel framework and are generally not expected to vary significantly with morphology or annealing temperature. Previous studies on $NiCo_2O_4$ prepared under different synthesis and annealing conditions have similarly reported consistent XPS peak positions for the spinel phase. Therefore, XPS analysis of NCO-5 is considered representative of the surface chemical states of the $NiCo_2O_4$ samples investigated in this work.

3.5. BET surface area and pore analysis

To examine the porous structure and specific surface area, nitrogen adsorption–desorption isotherms were measured for NCO-B and NCO-5. Both samples exhibit Type IV isotherms with H3-type hysteresis loops (Fig. 3), confirming mesoporous structures with slit-shaped pores consistent with their respective morphologies. The BET specific surface area and total pore volume of NCO-B were determined to be 388.15 $m^2\ g^{-1}$ and 1.37 $cm^3\ g^{-1}$, respectively, significantly higher than those of NCO-5 (68.06 $m^2\ g^{-1}$, 0.76 $cm^3\ g^{-1}$). However, micropore (MP) plot analysis reveals that NCO-B possesses a notable micropore volume ($\sim$0.095 $cm^3\ g^{-1}$), indicating that a substantial fraction

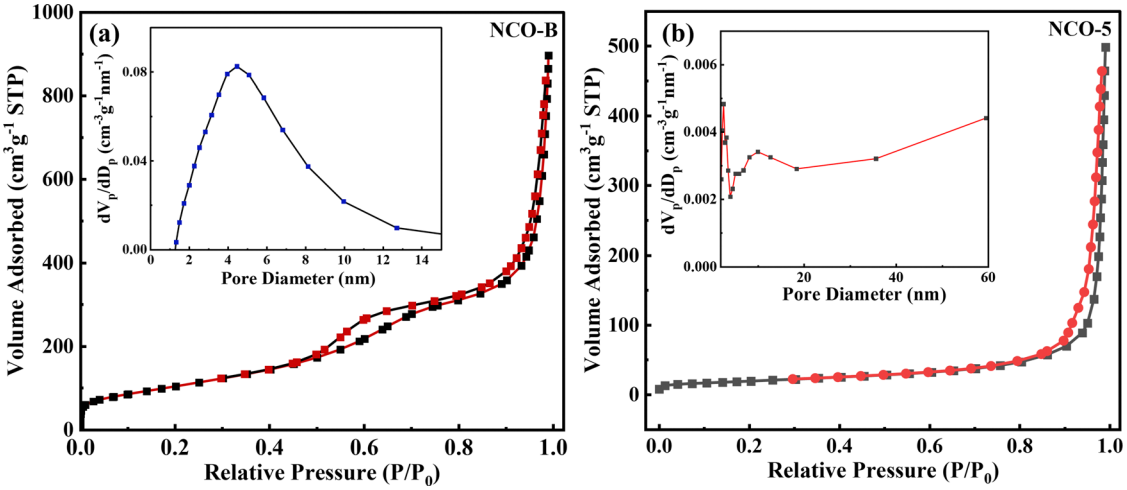

Fig. 3 Nitrogen adsorption–desorption isotherms of (a) NCO-B and (b) NCO-5. The inset shows the corresponding BJH pore size distribution curves.

of its surface area arises from micropores with diameters ~1.8 nm. In contrast, NCO-5 shows negligible microporosity, with its pore structure dominated by larger mesopores. The BJH average pore diameter of NCO-5 (46.47 nm) is approximately 3.8× larger than that of NCO-B (12.22 nm), while the BET average pore diameter follows the same trend (22.26 nm *vs.* 7.05 nm). The larger pore diameter of NCO-5 facilitates easier diffusion of p-nitrophenolate ions and BH_4^- to the catalytically active Ni and Co surface sites, while the predominantly microporous surface area of NCO-B is largely inaccessible to these reactant molecules. The higher BET constant (C) of NCO-5 (145.33 *vs.* 51.25 for NCO-B) further suggests stronger surface-adsorbate interactions at NCO-5 active sites. These results demonstrate that pore accessibility, active site availability, and surface-adsorbate interaction strength contribute to the catalytic performance rather than total surface area.

3.6. Catalytic activity

The catalytic reduction performance of the synthesized $NiCo_2O_4$ samples was evaluated through the conversion of PNP to PAP in the presence of $NaBH_4$ under different catalytic conditions. Prior to the catalytic experiments, control studies involving only $NaBH_4$ and only the NCO-5 catalyst without $NaBH_4$ were carried out, and the corresponding UV-vis spectral evolutions are provided in the SI (Fig. S1). In the absence of a catalyst, the reduction of PNP using only $NaBH_4$ proceeded very slowly and took around 150 minutes for complete reduction (Fig. S1(a)), indicating limited direct electron transfer between BH_4^- ions and PNP molecules. Similarly, the catalyst-alone (Fig. S1(b)) system under UV irradiation exhibited a lower conversion efficiency (62.5% in 90 minutes) under identical conditions, confirming the important role of $NaBH_4$ in facilitating the reduction process.

The time-dependent UV-vis spectral evolution for NCO-B, NCO-3, and NCO-5 is presented in Fig. 4(a–c). In all cases, the characteristic absorption peak of *p*-nitrophenolate ions at approximately 400 nm gradually decreased with reaction time, indicating the progressive reduction of PNP. Among the investigated samples, NCO-5 exhibited the fastest reduction rate, achieving nearly complete conversion within 13 min, whereas NCO-3 and NCO-B required approximately 18 and 20 min, respectively. The enhanced catalytic performance of NCO-5 demonstrates the significant influence of morphology evolution on catalytic activity.

The improved catalytic activity of NCO-5 may be attributed to its interconnected nanorod architecture, which enhances the accessibility of catalytically active sites and facilitates more efficient interfacial electron transfer during reduction. Although BET analysis (Fig. 3) revealed a comparatively higher surface area for NCO-B, the superior catalytic performance of NCO-5 suggests that catalytic activity is governed not only by surface area but also by morphology-dependent factors such as reactant diffusion pathways and charge-transfer efficiency.

Fig. 4(d) shows the UV-assisted catalytic reduction of PNP using NCO-5 in the presence of $NaBH_4$ under 254 nm UV irradiation. Under UV illumination, the reduction process was significantly accelerated, achieving nearly complete conversion within 7 min. The enhanced activity under UV irradiation may be associated with photo-assisted charge generation in $NiCo_2O_4$, which promotes more efficient electron transfer during the reduction reaction.[41]

Furthermore, the time-resolved UV-vis spectra in Fig. 4(a–d) show no absorption peaks at 320–330 nm or 240 nm at any time point during the reaction, ruling out the accumulation of nitrosobenzene and hydroxylaminobenzene, respectively, which are the two known partial reduction intermediates in the PNP to PAP pathway. The progressive and clean growth of the PAP peak at 300 nm confirms selective and complete reduction without detectable byproduct formation under the excess $NaBH_4$ conditions used.

The conversion efficiency plots shown in Fig. 4(e) further confirm the catalytic activity trend, following the order:

$$\text{NCO-B} < \text{NCO-3} < \text{NCO-5} < \text{NCO-5} + \text{UV}$$

The kinetic behavior of the catalytic reduction process was analysed using an apparent pseudo-first-order kinetic model with respect to PNP concentration, as shown in Fig. 4(f). Since $NaBH_4$ was employed in large excess relative to PNP, its concentration

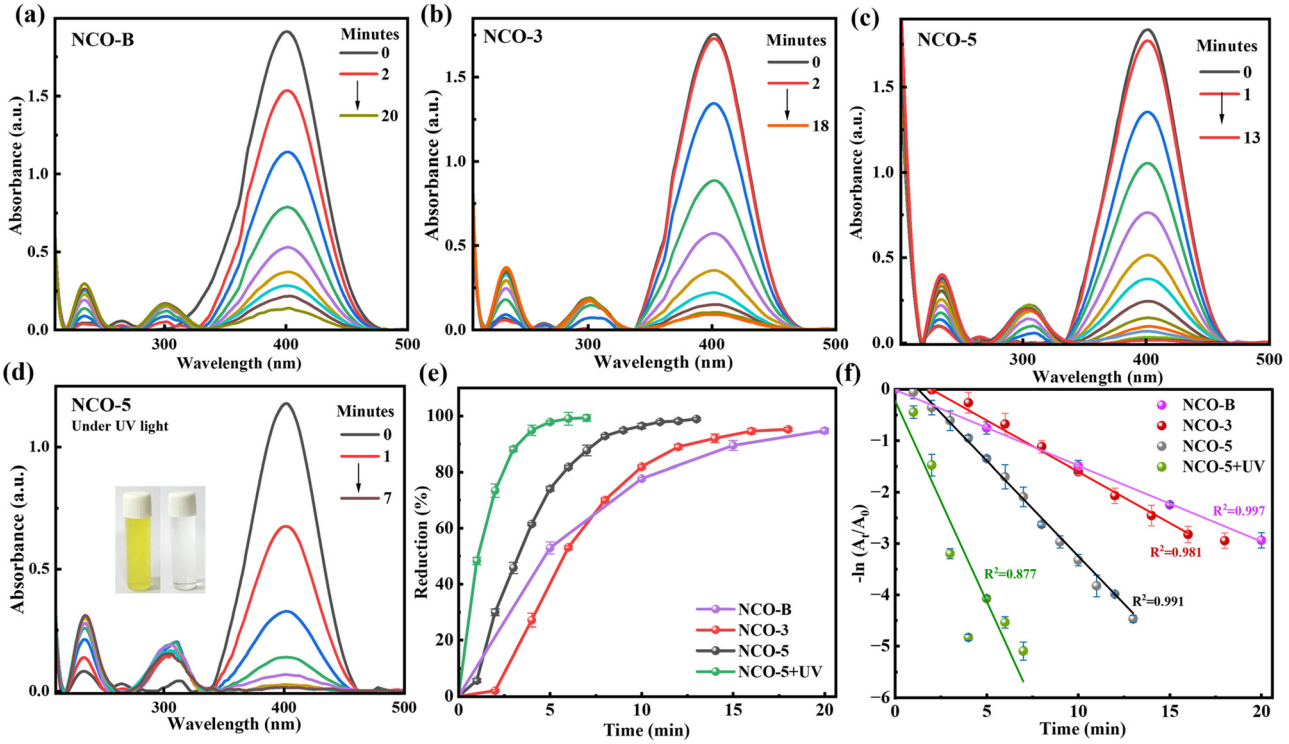

Fig. 4 Catalytic reduction of PNP using morphology-engineered $NiCo_2O_4$ samples: (a–c) time-dependent UV-vis spectral evolution of PNP reduction in the presence of NCO-B, NCO-3, and NCO-5 catalysts along with $NaBH_4$, respectively; (d) UV-vis spectral evolution of PNP reduction using NCO-5 and $NaBH_4$ under UV irradiation (inset: visual image showing the conversion of PNP to PAP); (e) conversion percentage of PNP under different catalytic conditions; (f) apparent pseudo-first-order kinetic plots [$\ln(C_t/C_0)$ *versus* time] for the catalytic reduction of PNP under different conditions.

was assumed to remain effectively constant during the reaction. The corresponding $\ln(C_t/C_0)$ *versus* time plots were linear for all catalytic systems, confirming the applicability of the apparent pseudo-first-order approximation. Among the investigated samples, NCO-5 under UV irradiation exhibited the highest apparent rate constant, followed by NCO-5, NCO-3, and NCO-B, respectively.

For optimization, the volumetric ratios of the dye, catalyst, and $NaBH_4$ were systematically varied as shown in Table 2. The condition 50–100–80 (PNP-NCO-$NaBH_4$ in μL) demonstrated the highest reduction rate, achieving 99.1% conversion in 13 minutes. This condition was more effective than the others, offering faster reaction and higher yield. Increasing the amount of catalyst or reducing agent beyond this point did not improve the outcome, likely due to limitations in reaction kinetics or the saturation of the catalyst's active sites.

Table 2 Catalytic conversion of PNP under varying reactant ratios

PNP (μL)	NCO (μL)	$NaBH_4$ (μL)	Conversion (%)	Time (min)
50	90	100	98.7	8
50	90	90	99.8	16
50	100	100	22.2	10
50	100	80	99.1	13
40	90	100	99.9	11
40	100	90	99.0	12

To quantitatively assess the catalytic performance of the optimized 50–100–80 (PNP-NCO-$NaBH_4$ in μL) condition, the reaction kinetics were evaluated using a pseudo-first-order model. As shown in Fig. S2(f), $-\ln(C_t/C_0)$ was plotted against time (t), where C_t and C_0 represent the concentrations of PNP at time t and the initial time, respectively.

For NCO-5, a strong linear correlation (R^2 = 0.9917) was observed, indicating that the reaction adheres to pseudo-first-order kinetics under the applied conditions. The slope of the linear fit yielded a rate constant (k) of 0.364 min^{-1}, which is considerably higher than the other optimally catalysed reductions. This high-rate constant demonstrates the remarkable efficiency of the $NiCo_2O_4$ catalyst in combination with $NaBH_4$ in accelerating the reduction of PNP to PAP.

Fig. S2 shows the conversion percentage and rate constant plots of all catalysts and the control reaction (only $NaBH_4$) under the same optimised conditions.

Similar studies were conducted under UV-light illumination (254 nm), and the results showed a further reduction in reduction time.[42] When the catalytic performance of the optimized 50–100–80 (PNP–NCO-5–$NaBH_4$ in μL) condition was evaluated under UV illumination, 99.51% reduction was observed in 7 minutes.

To further understand the conversion of PNP to PAP, FTIR spectra of the reaction solutions obtained before and after catalytic reduction using $NiCo_2O_4$ are presented in Fig. S3 (supplementary information, SI). The δ(C–H) aromatic bending vibration near 777 cm^{-1} and ν(C–O) stretching vibration around 1219 cm^{-1}

are retained in both spectra, indicating preservation of the aromatic phenolic framework during the reduction process. The characteristic $\nu(NO_2)$ vibration observed near 1500 cm^{-1} in PNP shows a marked reduction in intensity after catalysis, accompanied by the appearance of δ(N–H) bending near 1630 cm^{-1} in the PAP spectrum, indicating conversion of the nitro group to an amino group. In addition, the broader absorption feature observed in the ν(N–H +O–H) region for PAP compared to the relatively sharper ν(O–H) band in PNP further supports the formation of amino-containing products after catalytic reduction.

Table 3 compares the catalytic activity of NCO-5 nanorods with other state-of-the-art nanocatalysts used in PNP reduction. This highlights the potential of the synthesized nanorods as sustainable nanocatalysts.

To identify the active species involved in the catalytic reduction of PNP, radical scavenger experiments were carried out using ammonium oxalate (AO), *p*-benzoquinone (BQ), and isopropyl alcohol (IPA), which act as scavengers for holes (h^+), superoxide radicals ($^{\bullet}O_2^-$), and hydroxyl radicals ($^{\bullet}OH$), respectively. As shown in Fig. 5(a), the catalytic reduction efficiency was significantly suppressed in the presence of BQ and IPA compared to the reaction without scavengers. In the case of AO, only a slight decrease was observed. Among the investigated scavengers, BQ caused the maximum suppression in catalytic activity, indicating that superoxide radicals play a dominant role in the UV-assisted reduction process. The noticeable decrease observed with IPA further suggests the involvement of hydroxyl radicals during catalysis. In contrast, the relatively smaller change in catalytic performance in the presence of AO indicates that photogenerated holes have a comparatively lower contribution to the overall reaction. These results suggest that the enhanced catalytic activity under UV irradiation is mainly associated with reactive oxygen species generated through photo-assisted charge-transfer processes.

The stability and reusability of the optimized NCO-5 catalyst were evaluated through repeated catalytic reduction cycles of PNP under identical experimental conditions. After each cycle, the catalyst was recovered by centrifugation, thoroughly washed with distilled water and ethanol to remove residual reactants and products, and subsequently reused for the next catalytic cycle without additional treatment.

As shown in Fig. 5(b), the catalyst retained high catalytic activity over five successive cycles, with reduction efficiencies of 99.5%, 98.8%, 99.2%, 99.0%, and 97.1%, respectively. Only a slight decrease in catalytic performance was observed after repeated cycling, indicating good structural stability and resistance to deactivation under the investigated reaction conditions.

The small fluctuations in conversion efficiency between intermediate cycles are attributed to minor experimental variations associated with catalyst recovery, redispersion, and handling during repeated reuse experiments.

To further evaluate the structural stability of the catalyst after repeated catalytic operation, FESEM and XRD analyses were performed on the recycled NCO-5 catalyst after the fifth cycle, as shown in Fig. 5(c and d). The FESEM image reveals that the interconnected nanorod-like morphology is largely retained even after repeated catalytic cycles, indicating good morphological stability under the investigated reaction conditions. The corresponding EDS spectrum is given in Fig. S5 (SI). The XRD pattern of the recycled catalyst retained the characteristic diffraction peaks of spinel $NiCo_2O_4$, without noticeable impurity peaks or significant peak shifts, confirming the preservation of the crystalline phase after repeated catalytic cycles.

The photoelectrochemical properties of NCO-5 and NCO-B were investigated using PL spectroscopy, EIS, and Mott–Schottky analysis as given in Fig. S4 (SI). The PL emission spectra recorded under 275 nm excitation (Fig. S4(a)) show that both samples exhibit emission bands at ~420, ~470, and ~570 nm, attributed to near band edge transitions, oxygen vacancy defect states, and deep level defect emissions, respectively; NCO-5 displays significantly higher emission intensity, indicating a richer concentration of oxygen vacancies and redox-active surface sites.[49] The Nyquist plots (Fig. S4(b)) reveal a smaller semicircle for NCO-5 compared to NCO-B, confirming lower charge-transfer resistance and faster interfacial electron-transfer kinetics. The Mott–Schottky plots of NCO-5 and NCO-B (Fig. S4(c)) were obtained in 6 M KOH electrolyte using a Hg/HgO reference electrode at a fixed frequency of 1 kHz. The negative slopes observed for both samples confirm their p-type semiconductor nature, consistent with reported $NiCo_2O_4$ spinel structures.[50] The flat-band potentials were determined from the *x*-intercepts of the linear fits to be −0.016 V and −0.002 V *vs.* Hg/HgO, corresponding to +0.082 V and +0.096 V *vs.* NHE for NCO-5 and NCO-B, respectively (conversion: E(NHE) = E(Hg/HgO) + 0.098 V in 6 M KOH). The smaller slope magnitude of NCO-5 compared to NCO-B suggests a relatively higher charge-carrier density in the nanorod morphology, consistent with its lower charge-transfer resistance observed in EIS and superior catalytic performance. The band edge positions were estimated using the empirical Mulliken electronegativity approach,[51]

Table 3 Comparative catalytic performance of NCO-5 nanorods with recent nanocatalysts for $NaBH_4$-assisted PNP reduction

Catalyst system	Pollutant	Time (min)	Conversion (%)	K_{app} (min^{-1})	Ref.
NCO-5 BNRs	PNP	13	99.1	0.3644	This work
NCO-5 BNRs (UV)	PNP	7	99.51	0.7798	This work
Fe_3O_4@CS–AgNi (core–shell BMPs)	PNP	6	100	0.56	43
AgNi@ZnO nanocomposite	PNP	2–3	~100	0.852	44
$Ni_{0.5}Mn_{0.5}Co_2O_4$ NPs	PNP (0.4 M)	few min	>90	0.690	45
$NiCo_2O_4$ NPs	PNP	90	~100	—	46
4%Zn-1.5%Pd/NZVI	PNP (50 mg L^{-1})	1	~100	0.095	47
Zinc-doped cobalt oxide	PNP (0.13 mmol L^{-1})	8	100	0.4	48

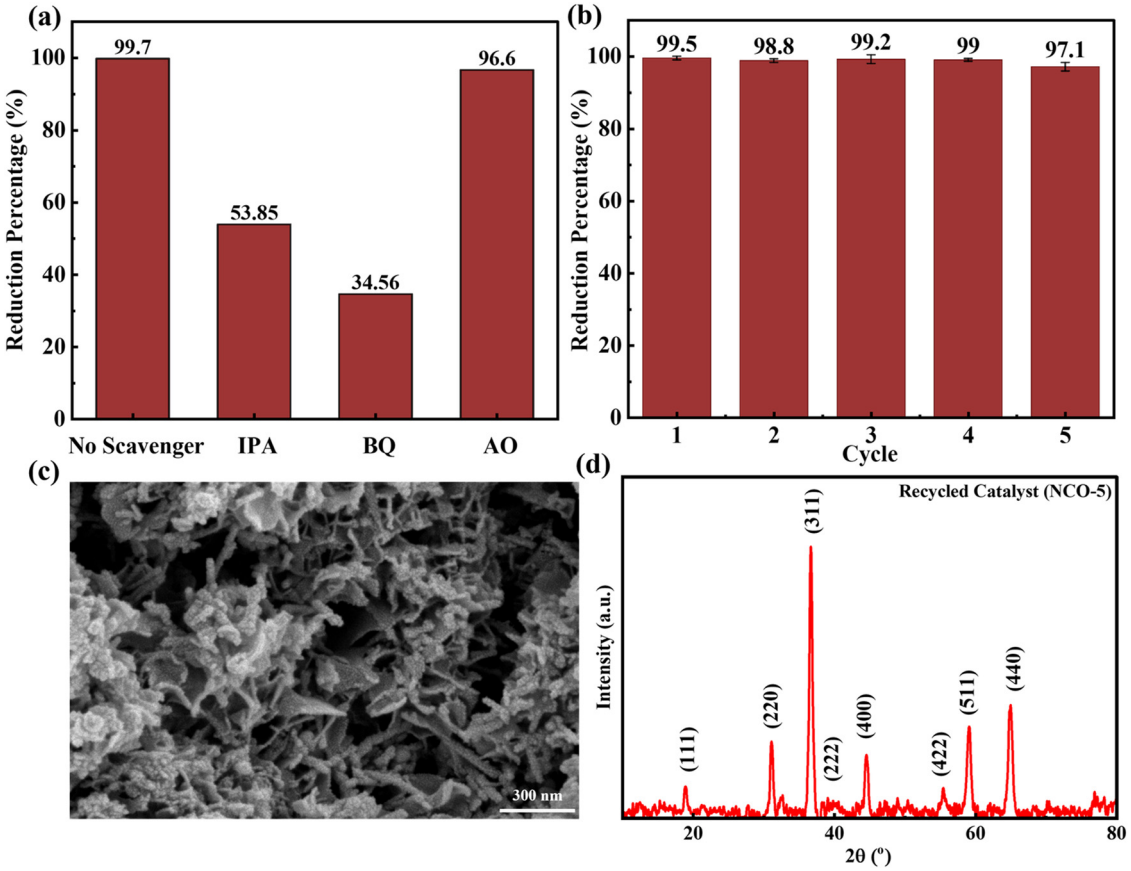

Fig. 5 (a) Scavenger trapping experiments during UV-assisted catalytic reduction of PNP using NCO-5 in the presence of ammonium oxalate (AO), *p*-benzoquinone (BQ), and isopropyl alcohol (IPA) showing reduction percentages; (b) reduction percentage *vs.* cycle number plot showing recyclability performance of NCO-5 over five successive catalytic cycles with corresponding error bars; (c) FESEM image and (d) XRD pattern of the recycled NCO-5 catalyst after 5 consecutive catalytic cycles.

yielding E_{CB} and E_{VB} of approximately −0.003 V and +2.90 V *vs.* NHE based on the optical bandgap of 2.9 eV. The E_{VB} position (+ 2.90 V *vs.* NHE) exceeds the $^{\bullet}OH/OH^{-}$ oxidation potential (+ 1.99 V *vs.* NHE), confirming thermodynamic feasibility of

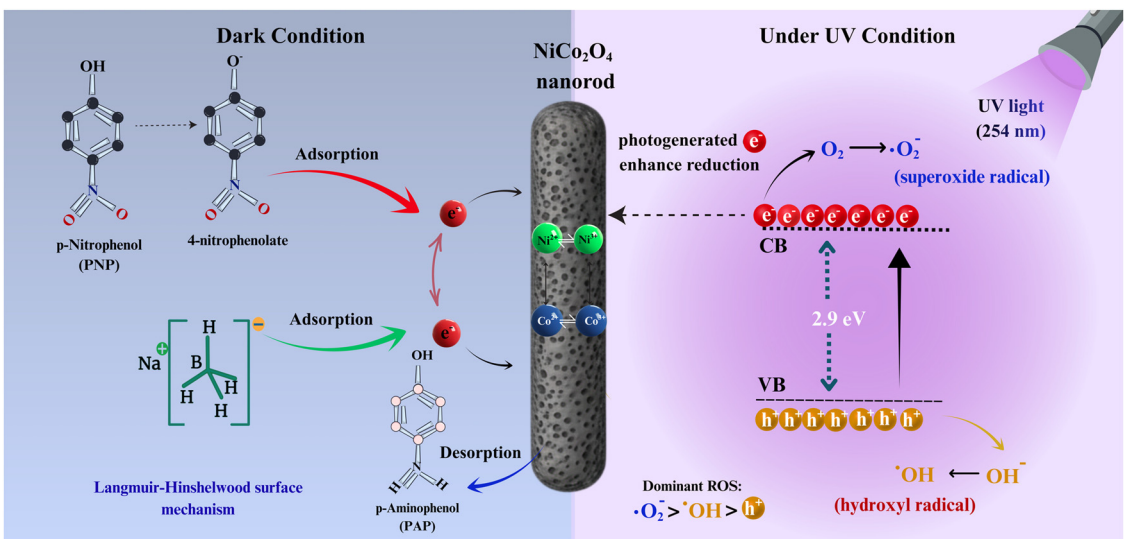

Scheme 2 Schematic illustration of the proposed Langmuir–Hinshelwood catalytic reduction mechanism of PNP over $NiCo_2O_4$ nanorods under dark and UV-irradiated conditions.

hydroxyl radical generation *via* photogenerated holes. Although the E_{CB} is in close proximity to the $O_2/^{\bullet}O_2^-$ reduction potential −0.33 V *vs*. NHE), superoxide radical generation likely proceeds *via* surface-mediated pathways facilitated by oxygen vacancy defect states, consistent with the dominance of $^{\bullet}O_2^-$ observed in scavenger experiments.

3.7. Mechanistic discussion

Scheme 2 shows the catalytic reduction of PNP to PAP over $NiCo_2O_4$ nanorods, which proceeds *via* a Langmuir–Hinshelwood surface mechanism. Upon the addition of $NaBH_4$, PNP transforms to *p*-nitrophenolate ions and adsorbs onto the catalyst surface. Here, interfacial electron transfer from BH_4^- (donor) to the adsorbed nitrophenolate (acceptor) drives the reduction to PAP, which subsequently desorbs from the catalyst surface. The mixed-valence Ni^{2+}/Ni^{3+} and Co^{2+}/Co^{3+} redox centres confirmed by XPS facilitate this electron relay, while the accessible pore structure of NCO-5 (pore size: 22.26 nm from BET) promotes efficient reactant diffusion to active sites.

Under UV irradiation, photogenerated electron–hole pairs in $NiCo_2O_4$ (p-type, E_g = 2.9 eV) may facilitate the formation of reactive oxygen species. The photogenerated charge carriers interact with oxygen and water molecules at the catalyst surface, generating superoxide ($^{\bullet}O_2^-$) and hydroxyl radicals ($^{\bullet}OH$). The conduction band position of NCO-5 is sufficiently negative relative to the $O_2/^{\bullet}O_2^-$ potential to thermodynamically support $^{\bullet}O_2^-$ generation. This is supported by the results earlier discussed in the Mott–Schottky analysis. Scavenger experiments suggest the relative contribution order of reactive species as $^{\bullet}O_2^- > {}^{\bullet}OH \gg h^+$, where the minor role of holes is attributed to the direct electron-donating action of BH_4^- in the reaction medium. The enhanced performance of NCO-5 under UV irradiation thus arises from the synergistic combination of surface-mediated electron transfer and photo-assisted generation of Reactive Oxygen Species (ROS).

4. Conclusions

Spinel $NiCo_2O_4$ nanorods derived from the thermal transformation of NiCo-layered double hydroxide at 500 °C exhibit enhanced catalytic activity for the reduction of PNP to PAP using $NaBH_4$. The optimized NCO-5 catalyst achieved 99.1% conversion within 13 min under dark conditions (k_{app} = 0.364 min^{-1}) and 99.5% conversion within 7 min under 254 nm UV irradiation (k_{app} = 0.779 min^{-1}). The improved catalytic performance is attributed to the nanorod morphology, accessible pore structure, and enhanced interfacial charge-transfer characteristics of the $NiCo_2O_4$ framework. Scavenger studies together with PL and EIS analyses further supported the role of photo-assisted charge transfer and reactive oxygen species generation during UV-assisted catalysis. The catalyst retained high catalytic activity after five successive cycles, demonstrating good operational stability and recyclability. The present study is limited to the reduction of a single model nitroaromatic pollutant under strongly alkaline conditions in the presence of excess $NaBH_4$, which may not fully represent practical wastewater environments. Future work should focus on evaluating catalyst performance in complex wastewater systems, in continuous-flow operation, and under visible-light-assisted catalytic conditions. Overall, the results demonstrate the potential of morphology-engineered bimetallic oxides for catalytic reduction of nitroaromatic pollutants.

Author contributions

Nanditha T. K.: designing and planning the study, writing – original draft, methodology, investigation, formal analysis, writing – review & editing. Mahi Varza Nataraajan: writing – original draft, methodology, investigation, formal analysis, writing – review & editing. Shreepooja Bhat: writing – original draft, methodology, investigation, formal analysis, writing – review & editing. Arun Kumar Thilipan: writing – review & editing, supervision, formal analysis, data curation, conceptualization. Raghavendra K. G. and Gurumurthy S. C.: writing – review & editing, supervision, data curation, conceptualization.

Conflicts of interest

The authors declare that they have no known competing financial interests or personal relationships that could have influenced the work reported in this paper.

Data availability

The data supporting this article have been included as part of the supplementary information (SI). Supplementary information is available. See DOI: https://doi.org/10.1039/d6ma00196c.

Acknowledgements

All the authors are greatly indebted to their respective organizations. Nanditha T K, Mahi Varza Natarajan, Shreepooja Bhat, Raghavendra K G and Gurumurthy S C acknowledge Manipal Academy of Higher Education for the funding support. During the preparation of this work, the authors used ChatGPT to improve language and readability. The authors reviewed and edited the content and take full responsibility for the publication's content. The use of ChatGPT was limited to language enhancement and did not influence the scientific content, data interpretation, or conclusions.

References

1 Y. Wu, *et al.*, The plant-growth promoting bacteria promote cadmium uptake by inducing a hormonal crosstalk and lateral root formation in a hyperaccumulator plant Sedum alfredii, *J. Hazard. Mater.*, 2020, **395**, 122661, DOI: 10.1016/j.jhazmat.2020.122661.
2 Q. Zhang, *et al.*, Multi-catalysis of glow discharge plasma coupled with FeS_2 for synergistic removal of antibiotic,

Chemosphere, 2023, **312**, 137204, DOI: 10.1016/j.chemosphere.2022.137204.

3 A. Negash, S. Mohammed, H. D. Weldekirstos, A. D. Ambaye and M. Gashu, Enhanced photocatalytic degradation of methylene blue dye using eco-friendly synthesized rGO@ZnO nanocomposites, *Sci. Rep.*, 2023, **13**(1), 22234, DOI: 10.1038/s41598-023-48826-7.

4 Md. T. Islam, *et al.*, Selectivity of Sol-Gel and Hydrothermal TiO_2 Nanoparticles towards Photocatalytic Degradation of Cationic and Anionic Dyes, *Molecules*, 2023, **28**(19), 6834, DOI: 10.3390/molecules28196834.

5 S. Khan, T. Noor, N. Iqbal and L. Yaqoob, Photocatalytic Dye Degradation from Textile Wastewater: A Review, *ACS Omega*, 2024, **9**(20), 21751–21767, DOI: 10.1021/acsomega.4c00887.

6 C. Tuc Altaf, *et al.*, Impact on the Photocatalytic Dye Degradation of Morphology and Annealing-Induced Defects in Zinc Oxide Nanostructures, *ACS Omega*, 2023, **8**(17), 14952–14964, DOI: 10.1021/acsomega.2c07412.

7 R. Tomar, A. A. Abdala, R. G. Chaudhary and N. B. Singh, Photocatalytic degradation of dyes by nanomaterials, *Mater. Today Proc.*, 2020, **29**, 967–973, DOI: 10.1016/j.matpr.2020.04.144.

8 V. Jawale, *et al.*, 6, 13-pentacenequinone/zinc oxide nanocomposites for organic dye degradation, *Mater. Today Proc.*, 2022, **52**, 17–20, DOI: 10.1016/j.matpr.2021.10.098.

9 I. R. Chowdhury, S. Chowdhury, M. A. J. Mazumder and A. Al-Ahmed, Removal of lead ions (Pb^{2+}) from water and wastewater: a review on the low-cost adsorbents, *Appl. Water Sci.*, 2022, **12**(8), 185, DOI: 10.1007/s13201-022-01703-6.

10 H. P. T. Shakila, H. R. Kavitha and A. P. Bupani, Adsorption Study of Cu^{2+} Ions from Aqueous Solutions by Bael Flowers (Aegle marmelos), *Biointerface Res. Appl. Chem.*, 2020, **11**(4), 11891–11904, DOI: 10.33263/BRIAC114.1189111904.

11 B. Murtaza, *et al.*, Novel design of Fe^0-and AC-doped hydroxyapatite-alginate composites for efficient arsenic clean-up: Mechanistic insights from batch and column tests, *J. Environ. Manage.*, 2026, **405**, 129634, DOI: 10.1016/j.jenvman.2026.129634.

12 M. S. Khan, Y. Li, D.-S. Li, J. Qiu, X. Xu and H. Y. Yang, A review of metal–organic framework (MOF) materials as an effective photocatalyst for degradation of organic pollutants, *Nanoscale Adv.*, 2023, **5**(23), 6318–6348, DOI: 10.1039/D3NA00627A.

13 K. Li, Y. de Rancourt de Mimérand, X. Jin, J. Yi and J. Guo, Metal Oxide (ZnO and TiO_2) and Fe-Based Metal–Organic-Framework Nanoparticles on 3D-Printed Fractal Polymer Surfaces for Photocatalytic Degradation of Organic Pollutants, *ACS Appl. Nano Mater.*, 2020, **3**(3), 2830–2845, DOI: 10.1021/acsanm.0c00096.

14 P. Falcaro, *et al.*, Application of metal and metal oxide nanoparticles@MOFs, *Coord. Chem. Rev.*, 2016, **307**, 237–254, DOI: 10.1016/j.ccr.2015.08.002.

15 J. Rani, *et al.*, Bimetallic nanoparticles as pioneering eco-friendly catalysts for remediation of pharmaceuticals and personal care products (PPCPs), *Nanoscale Adv.*, 2025, **7**(11), 3160–3188, DOI: 10.1039/D5NA00151J.

16 Y. Quan, L. Peng, Y. Jin, S. Wu, J. Zhao and J. Ren, Highly effective chainlike Ni/CZ5-x catalysts for catalytic reduction of p-nitrophenol: Effect of Si/Al ratio of ZSM-5 support, *J. Environ. Chem. Eng.*, 2023, **11**(6), 111402, DOI: 10.1016/j.jece.2023.111402.

17 H. K. Brown, *et al.*, Synthesis and Catalytic Activity for 2, 3, and 4-Nitrophenol Reduction of Green Catalysts Based on Cu, Ag and Au Nanoparticles Deposited on Polydopamine-Magnetite Porous Supports, *Nanomaterials*, 2023, **13**(15), 2162, DOI: 10.3390/nano13152162.

18 A. O. Cardoso Juarez, E. Ivan Ocampo Lopez, M. K. Kesarla and N. K. R. Bogireddy, Advances in 4-Nitrophenol Detection and Reduction Methods and Mechanisms: An Updated Review, *ACS Omega*, 2024, **9**(31), 33335–33350, DOI: 10.1021/acsomega.4c04185.

19 Y. M. Hunge, A. A. Yadav, S.-W. Kang, H. Kim, A. Fujishima and C. Terashima, Nanoflakes-like nickel cobaltite as active electrode material for 4-nitrophenol reduction and supercapacitor applications, *J. Hazard. Mater.*, 2021, **419**, 126453, DOI: 10.1016/j.jhazmat.2021.126453.

20 S. M. Padre, *et al.*, Mono- and Bimetallic Nanoparticles for Catalytic Degradation of Hazardous Organic Dyes and Antibacterial Applications, *ACS Omega*, 2022, **7**(39), 35023–35034, DOI: 10.1021/acsomega.2c03784.

21 M. Sankar, N. Dimitratos, P. J. Miedziak, P. P. Wells, C. J. Kiely and G. J. Hutchings, Designing bimetallic catalysts for a green and sustainable future, *Chem. Soc. Rev.*, 2012, **41**(24), 8099, DOI: 10.1039/c2cs35296f.

22 T. U. Rahman, M. R. Dihan, A. Hai and Md. S. Islam, Enhanced photodegradation of antibiotics using a novel $BiVO_4$/P-doped TiO_2 heterostructure: performance evaluation, property and kinetic modelling, *Mater. Adv.*, 2026, **7**, 2892–2910, DOI: 10.1039/D5MA01398D.

23 M. P. Shilpa, *et al.*, Nanogold-decorated reduced graphene oxide for catalytic hydrogenation of 4-nitrophenol, *Mater. Chem. Phys.*, 2023, **307**, 128145, DOI: 10.1016/j.matchemphys.2023.128145.

24 M. Srinivas, C. P. Prathibha, D. Yashaswini, P. Indhushree and M. R. Lavanya, Synthesis of binary $NiCo_2O_4$/ZnO composites as efficient photocatalysts for methylene blue degradation under visible light, *RSC Applied Interfaces*, 2026, **3**, 125–134, DOI: 10.1039/D5LF00226E.

25 H. Ali, W. M. A. El Rouby, M. H. Khedr and M. F. M. Hmamm, Enhanced electrocatalytic performance of $NiCo_2O_4$ nanosheets and nanoribbons for methanol oxidation in alkaline media: morphology-dependent insights, *Nanoscale Adv.*, 2025, **7**(16), 5080–5092, DOI: 10.1039/D5NA00223K.

26 K. Ajravat, A. Gupta, O. P. Pandey and L. K. Brar, Tailoring synthesis parameters of $NiCo_2O_4$ nanorods for enhanced supercapacitive performance, *Chem. Eng. Commun.*, 2025, **212**(9), 1323–1331, DOI: 10.1080/00986445.2025.2460489.

27 G. Kerherve, *et al.*, KherveFitting: An Open Source Software for Fitting X-Ray Photoelectron Spectroscopy Data, *Surf. Interface Anal.*, 2026, **58**(1), 54–65, DOI: 10.1002/sia.70032.

28 Z. Ju, G. Ma, Y. Zhao, Z. Xing, Y. Qiang and Y. Qian, A Facile Method for Synthesis of Porous $NiCo_2O_4$ Nanorods as a High-Performance Anode Material for Li-Ion Batteries, *Part. Part. Syst. Charact.*, 2015, **32**(11), 1012–1019, DOI: 10.1002/ppsc.201500093.

29 Y. Li, *et al.*, Ultrathin hollow-structured $NiCo_2O_4$ nanorod supported on improved N-doped graphene for superior supercapacitor applications, *J. Alloys Compd.*, 2017, **722**, 903–912, DOI: 10.1016/j.jallcom.2017.06.138.
30 X. Wang, *et al.*, Controllable Synthesis of NiCo LDH Nanosheets for Fabrication of High-Performance Supercapacitor Electrodes, *Electroanalysis*, 2017, **29**(5), 1286–1293, DOI: 10.1002/elan.201600602.
31 M. Sethi and D. K. Bhat, Facile solvothermal synthesis and high supercapacitor performance of $NiCo_2O_4$ nanorods, *J. Alloys Compd.*, 2019, **781**, 1013–1020, DOI: 10.1016/j.jallcom.2018.12.143.
32 Y. Mehdizadeh, *et al.*, Ultra-broadband microwave absorption performance of multi-scale designed Fe_3O_4 @$NiCo_2O_4$/PANI/NRGO aerogels, *J. Mater. Chem. A Mater.*, 2025, **13**(29), 23766–23785, DOI: 10.1039/D5TA03371C.
33 S. Bae, S. Gim, H. Kim and K. Hanna, Effect of $NaBH_4$ on properties of nanoscale zero-valent iron and its catalytic activity for reduction of p-nitrophenol, *Appl. Catal., B*, 2016, **182**, 541–549, DOI: 10.1016/j.apcatb.2015.10.006.
34 C. Mahala and M. Basu, Nanosheets of $NiCo_2O_4$/NiO as Efficient and Stable Electrocatalyst for Oxygen Evolution Reaction, *ACS Omega*, 2017, **2**(11), 7559–7567, DOI: 10.1021/acsomega.7b00957.
35 B. Shreepooja, T. K. Nanditha, B. Namitha, P. Rajashekhar, S. Surabhi and S. C. Gurumurthy, Green-synthesized Ag-Ag_2S Heterostructures for efficient catalytic remediation of 4-Nitrophenol, *Mater. Res. Bull.*, 2026, **194**, 113732, DOI: 10.1016/j.materresbull.2025.113732.
36 R. U. Amate, M. K. Bhosale, P. J. Morankar, A. M. Teli and C.-W. Jeon, Polyvinylpyrrolidone-Functionalized $NiCo_2O_4$ Electrodes for Advanced Asymmetric Supercapacitor Application, *Polymers*, 2025, **17**(13), 180210.3390/polym17131802.
37 B. Cui, *et al.*, Photophysical and Photocatalytic Properties of Core-Ring Structured $NiCo_2O_4$ Nanoplatelets, *J. Phys. Chem. C*, 2009, **113**(32), 14083–14087, DOI: 10.1021/jp900028t.
38 L. Isac, L. Andronic, M. Visa and A. Enesca, Selective photocatalytic degradation of organic pollutants by Cu_xS/ZnO/TiO_2 heterostructures, *Ceram. Int.*, 2020, **46**(4), 4265–4273, DOI: 10.1016/j.ceramint.2019.10.147.
39 V. K. Sharma and H. V. Demir, Bright Future of Deep-Ultraviolet Photonics: Emerging UVC Chip-Scale Light-Source Technology Platforms, Benchmarking, Challenges, and Outlook for UV Disinfection, *ACS Photonics*, 2022, **9**(5), 1513–1521, DOI: 10.1021/acsphotonics.2c00041.
40 A. Sotnikova, M. Ivantsov, A. Kulikov and M. Kulikova, Influence of MgO promoution to Ni-based composites in hydrogen production methane decomposition process, *Int. J. Hydrogen Energy*, 2024, **57**, 1208–1220, DOI: 10.1016/j.ijhydene.2024.01.123.
41 S. Zhang, *et al.*, Self-standing photo-assisted $NiCo_2O_4$/Cu_2O electrode with boosted energy storage performance by an ultra-simple approach, *Appl. Surf. Sci.*, 2025, **698**, 163113, DOI: 10.1016/j.apsusc.2025.163113.
42 S. Rao, *et al.*, Zn-doped TiO_2 nanoparticles: enhanced catalytic and nonlinear optical properties, *J. Mater. Sci.: Mater. Electron.*, 2025, **36**(19), 1144, DOI: 10.1007/s10854-025-15182-3.
43 R. Antony, R. Marimuthu and R. Murugavel, Bimetallic Nanoparticles Anchored on Core–Shell Support as an Easily Recoverable and Reusable Catalytic System for Efficient Nitroarene Reduction, *ACS Omega*, 2019, **4**(5), 9241–9250, DOI: 10.1021/acsomega.9b01023.
44 A. P. Sachi, A. P. Singh and M. Thirumal, Fabrication of AgNi Nano-alloy-Decorated ZnO Nanocomposites as an Efficient and Novel Hybrid Catalyst to Degrade Noxious Organic Pollutants, *ACS Omega*, 2021, **6**(50), 34771–34782, DOI: 10.1021/acsomega.1c05266.
45 U. Pal, F. E. Cancino-Gordillo and J.-L. Ortiz-Quiñonez, Rapid Nitrophenol Degradation Using Gel-Combustion Synthesized Nickel/Manganese Cobaltite (Ni1-Xmnxco2o4) Nanoparticles, *Appl. Surf. Sci.*, 2024, **659**, 159873, DOI: 10.1016/j.apsusc.2024.159873.
46 T. Swathi and G. Buvaneswari, Application of $NiCo_2O_4$ as a catalyst in the conversion of p-nitrophenol to p-aminophenol, *Mater. Lett.*, 2008, **62**(23), 3900–3902, DOI: 10.1016/j.matlet.2008.05.028.
47 G. Tokazhanov, S. Han and W. Lee, Enhanced catalytic reduction of p-nitrophenol by nano zerovalent iron - supported metal catalysts, *Catal. Commun.*, 2021, **158**, 106337, DOI: 10.1016/j.catcom.2021.106337.
48 M. Lu, *et al.*, Efficient and Stable Degradation of *p*-Nitrophenol over Zinc-Doped Cobalt Oxide for Wastewater Treatment, *Ind. Eng. Chem. Res.*, 2026, **65**(1), 291–299, DOI: 10.1021/acs.iecr.5c04052.
49 A. Gandhi and S. Wu, Strong Deep-Level-Emission Photoluminescence in NiO Nanoparticles, *Nanomaterials*, 2017, **7**(8), 231, DOI: 10.3390/nano7080231.
50 S. Kizhepat, A. S. Rasal, G. G. Demissie, V. Gurav, A. V. Ghule and J.-Y. Chang, Unveiling the impact of Mott-Schottky n-n junction in $NiCo_2O_4$/$Co(OH)_2$FeOOH heterostructure for enhanced supercapacitor performance, *J. Power Sources*, 2025, **649**, 237435, DOI: 10.1016/j.jpowsour.2025.237435.
51 M. A. Butler and D. S. Ginley, Prediction of Flatband Potentials at Semiconductor-Electrolyte Interfaces from Atomic Electronegativities, *J. Electrochem. Soc.*, 1978, **125**(2), 228–232, DOI: 10.1149/1.2131419.